applied optics

Effects of small misalignments on the intensity and Strehl ratio for a laser beam focused by an off-axis parabola

Luca Labate,[1,2,*] Paolo Ferrara,[1] Lorenzo Fulgentini,[1] and Leonida A. Gizzi[1,2]

[1]Istituto Nazionale di Ottica, Consiglio Nazionale delle Ricerche, via Moruzzi 1, 56124 Pisa, Italy
[2]Istituto Nazionale di Fisica Nucleare, Sezione di Pisa, largo B. Pontecorvo 3, 56127 Pisa, Italy
*Corresponding author: luca.labate@ino.it

Received 6 May 2016; revised 18 July 2016; accepted 18 July 2016; posted 22 July 2016 (Doc. ID 263874); published 10 August 2016

A general procedure is described to calculate the intensity and Strehl ratio, at a generic plane in the focal region, of a beam focused by an off-axis parabolic mirror in the presence of small misalignments. The general theoretical framework is first developed, which allows a full vector diffraction treatment in the case of general misalignments. Then, a parametric numerical study is reported, aimed at highlighting the tolerances of both the intensity and Strehl ratio for small misalignments, for different focusing and off-axis parabola parameters. A set of experimental measurements aimed at validating the theoretical model is also discussed. © 2016 Optical Society of America

OCIS codes: (140.7090) Ultrafast lasers; (230.4040) Mirrors; (350.5400) Plasmas.

http://dx.doi.org/10.1364/AO.55.006506

1. INTRODUCTION

Off-axis parabolic mirrors (OAPs) have now become essential devices to focus ultrashort ($\lesssim$100 fs duration) laser pulses up to relativistic ($\gtrsim 10^{18}$ W/cm^2) intensities without the undesired nonlinear and dispersive effects induced on the pulsed beam by transmissive focusing optics [1].

As it is well known, parabolic mirrors fall in the limited class of optical devices able to focus, in the ray optics approximation, a parallel beam onto a single point, thus allowing high numerical aperture optical systems to be developed based upon them with potentially no aberrations. For this reason, parabolic mirrors have been used for a long time for optical and, more recently, x-ray astronomy [2,3]. Moreover, the use of parabolic mirrors is being increasingly considered for usage in high resolution optical microscopy [4–7].

A general theoretical/numerical treatment aimed at characterizing the e.m. field distribution in the focal plane of a parabolic mirror in an on-axis configuration was given by Varga and Török in [8,9], in the context of optical microscopy. One of their main conclusions is that high numerical aperture focusing may lead to strong intensity variations at different positions across the focal plane. However, although an ideal 4π focusing is very demanding in terms of optical quality and thus manufacturing process, it has been experimentally verified that a confocal microscope using a high numerical aperture parabolic mirror can deliver excellent images with only small deviations from the calculated ideal case [10,11]. Finally, we mention here that noteworthy results were obtained, in the context of confocal microscopy, in terms of small focal spot size, using radially polarized light beams focused by parabolic mirrors [12,13]. All of the above applications typically employ parabolic mirrors in the on-axis configuration.

As said above, the usage of parabolic mirrors in an off-axis configuration has enabled the unique properties of ultrashort, powerful ($\gtrsim$1 TW) laser pulses to be fully exploited in ultraintense laser–matter interaction. This allowed novel research fields to be opened, such as, for instance, the development of ultrashort x-ray sources and proton/ion acceleration from laser–solid interactions (see [14] and References therein) or of laser-driven electron accelerators and secondary sources from laser–gas interactions (see [15,16] and References therein). In these cases, off-axis parabolic mirrors with f numbers ranging from $\gtrsim$1 up to $\approx$20–50 are most commonly employed, with unfocused laser beam transverse size (setting the OAP size) ranging from a few tens of millimeters for the TW-scale lasers up to a few hundreds of millimeters for sub-PW to PW scale systems.

In this paper, we report on a theoretical/numerical work, based upon a full vector diffraction treatment, aimed at characterizing the structure of a laser beam in the vicinity of the focal region of an off-axis parabola in the presence of misalignments of the incoming beam, with particular attention to parabolic mirror configurations typically encountered in the field of intense laser interaction with matter. In particular, rather than considering the characterization of the far-field aberrations, we mainly focus our attention on the achievable

maximum intensity and energy encircled in the focal spot in the presence of small misalignments. Our analysis will be also valid (and a few numerical cases will be discussed) for generic planes across the focus, in a spatial extent of a few Rayleigh lengths. In contrast to the case of optical microscopy, a knowledge of the intensity away from the focus is of a greater importance in the context of intense laser–matter interaction. In the case of the laser interaction with a solid target, for example, due to an amplified spontaneous emission pedestal and/or to the picosecond prepulse, a pre-plasma can develop in front of the target surface, leading to the main interaction taking place slightly before the focal plane. Moreover, in some context, a slight defocus is intentionally introduced in order to reduce the intensity and/or increase the spot size [17–19]. Also, in the context of laser interaction with gas targets, it is not easy to produce and/or identify a steep density gradient in the gas distribution, so that the laser pulse actually starts interacting with the target slightly before getting focused. To our best knowledge, although a vast literature dealing with the optics of parabolic mirrors exists, in particular, as said above, in typical configurations used in astronomy and microscopy, a work aimed at investigating the effects of possible small misalignments on those parameters of interest in the context of high-intensity laser–matter interaction is still missing.

As a matter of fact, the first paper dealing with the imaging/focusing properties of off-axis parabolic mirrors dates back to 1979 [20], where the intensity distribution in the focus was studied in the framework of ray optics. The diffraction pattern in the focal plane of an OAP mirror was studied in [21], while a ray-tracing approach was undertaken by Arguijo and Scholl [22], considering a tilted incident beam as well. A ray-tracing approach was also used in [23] to calculate the inherent aberrations in the case of a perfectly aligned OAP. The e.m. field in the focal region of an on-axis parabolic mirror used in confocal imaging of small nanoparticles and single molecules was studied in [11], where the effects of small misalignments were also considered; the authors showed that small misalignment angles δ (of the order of a few πkf, k being the wavenumber and f the focal length) give rise to a strong coma in the focal region. Such a conclusion was also drawn in [24], where the intensity distribution of a TM_{01} beam focused by a parabolic mirror was studied in the framework of the Richards–Wolf diffraction theory. From the experimental viewpoint, a procedure to perfectly align an OAP mirror, along with a characterization of the focal plane aberrations, was reported in [25]. Restricting our attention to the field of ultraintense laser–matter interaction, Bahk *et al.* [26] reported on the characterization and corrections, by means of a wavefront sensor and adaptive mirror, of the aberrations in the focal plane produced by a high numerical aperture OAP, aimed at reaching an ultrahigh intensity of the order of 10^{22} W/cm^2.

In what follows, we first lay down a general theoretical framework, based upon the Stratton–Chu vector diffraction theory [27], for the calculation of the intensity distribution of a super-Gaussian laser beam focused by an OAP in the presence of possible misalignments. In other words, we account for the incoming laser beam direction being not perfectly parallel to the OAP axis. Afterwards, we consider selected cases of OAP focusing and misalignments, concentrating our attention on the effects induced on the maximum intensity and the energy encircled in the main focal spot. Finally, we report on a set of experimental measurements aimed at checking the soundness of the theoretical model.

2. GENERAL THEORETICAL FORMULATION

We consider a Cartesian coordinate system as depicted in Fig. 1, that is, with the origin in the parent paraboloid vertex, the z axis lying along the paraboloid axis of symmetry, oriented such that the focus position is $\mathbf{x}_F = (0, 0, z_F)$, with $z_F = f > 0$. Furthermore, the x direction lies in the meridional plane, that is, the plane of the optical axis and the wavevector of a perfectly aligned incident beam at its center (to be better defined below). The equation of the parent paraboloid can thus be written as

$$z = g(x, y) = a(x^2 + y^2) \equiv s(x, y) \cdot f, \tag{1}$$

with $a = 1/4f$, f being the parent focal length, and we have defined the function $s(x, y) = \frac{a}{f}(x^2 + y^2) = (x^2 + y^2)/4f^2$, which will be useful in the following. The region of the parent paraboloid making up the off-axis parabola mirror surface is identified by the inequality

$$\text{OAP: } (x - d_{\text{OAD}})^2 + y^2 \le d^2, \tag{2}$$

where d_{OAD} is the so-called off-axis distance (see, for instance, [28]), and d is the diameter (or, from a practical viewpoint, the clear aperture). In Section 3 the value of the off-axis angle will also be used; it can be easily calculated as $\vartheta_{\text{OA}} = d_{\text{OAD}}/(f - ad_{\text{OAD}}^2)$.

In order to calculate the field in the region close to the focal position, we use the vector formulation of the diffraction

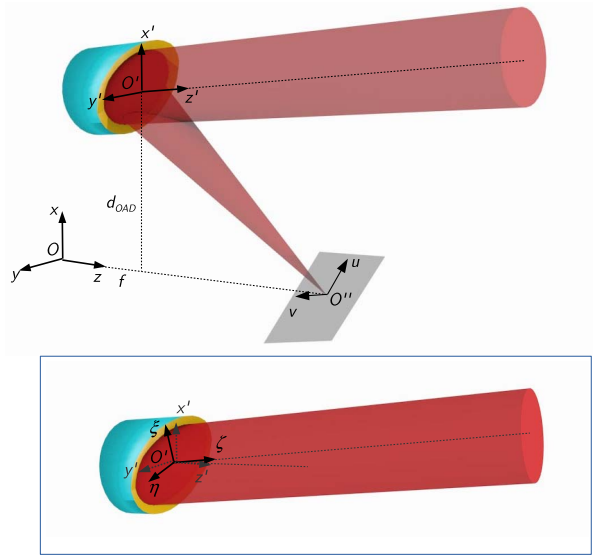

Fig. 1. Sketch of the different coordinate systems used throughout the paper. The origin of the $Oxyz$ system lies in the vertex position of the parent paraboloid. The $O'x'y'z'$ system is obtained from the corresponding unprimed system by a translation of the origin to the center of the OAP. The axis z and z' are parallel to the direction of a perfectly aligned beam. In the inset, a misaligned beam and the corresponding coordinate system are sketched (see text).

integral given by Stratton and co-workers [27,29]. We will follow a similar approach to that undertaken in [26] [so that Eqs. (3)–(10) will be similar to those in that paper], but we will generalize these calculations to the case of an incoming beam having a generic direction. Thus, we first calculate the fields on the OAP surface and then we use these quantities for calculating the Stratton–Chu integrals, which provide the electric and magnetic fields at the point $\mathbf{x}_P$ in the far field:

$$\mathbf{E}(\mathbf{x}_P) = \frac{1}{4\pi}\int_{\mathrm{OAP}} [ik(\hat{\mathbf{n}}\times\mathbf{B})G + (\hat{\mathbf{n}}\times\mathbf{E})\times\nabla G + (\hat{\mathbf{n}}\cdot\mathbf{E})\nabla G]\mathrm{d}A, \tag{3}$$

$$\mathbf{B}(\mathbf{x}_P) = \frac{1}{4\pi}\int_{\mathrm{OAP}} [ik(\mathbf{E}\times\hat{\mathbf{n}})G + (\hat{\mathbf{n}}\times\mathbf{B})\times\nabla G + (\hat{\mathbf{n}}\cdot\mathbf{B})\nabla G]\mathrm{d}A, \tag{4}$$

where $k = 2\pi/\lambda$ is the wavenumber, $\hat{\mathbf{n}}$ is the inward normal to the paraboloid surface (that is, directed from the surface toward the focal region), and G is the Green function for the Helmholtz equation

$$G(\mathbf{x}) = G(\mathbf{x}-\mathbf{x}_P) = \frac{e^{ik|\mathbf{x}-\mathbf{x}_P|}}{|\mathbf{x}-\mathbf{x}_P|}. \tag{5}$$

The integration is carried out on the surface of the OAP, identified by the Eqs. (1) and (2). With respect to the original formulation of the Stratton–Chu integrals, we have dropped here the additional term involving a line integral along the OAP contour, since it was demonstrated to give a negligible contribution to the far field (see [8] and [26]).

Notice that we will be using, throughout the following reasoning, the so-called "Gaussian" system of units (see, for instance, [29]). We will also be assuming nonmagnetic media, so that, in the Gaussian system, $\mu = 1$ and $\mathbf{B} = \mathbf{H}$. We also notice that the original Stratton–Chu formulas (3) and (4) have to be written in terms of $\mathbf{H}$ instead of $\mathbf{B}$. Thus, in order to convert all the formulas of this paper to the SI system of units, the following two-step procedure may be used: (1) replace $\mathbf{B}$ with $\mathbf{H}$; (2) replace $\mathbf{E}$ with $\sqrt{4\pi\epsilon_0}\mathbf{E}$ and $\mathbf{H}$ with $\sqrt{4\pi\mu_0}\mathbf{H}$, ϵ_0 and μ_0 being the vacuum electric permittivity and magnetic permeability.

The electric and magnetic fields appearing in Eqs. (3) and (4) as boundary conditions on the OAP surface were discussed by Varga and Török in [8] (see also [26]); starting from the condition that they are to be considered as the sum of the incident and reflected fields and assuming a perfect (that is, 100%) reflection, they showed that $\mathbf{E}$ and $\mathbf{B}$ can be written as a function of the incident fields $\mathbf{E}_i$ and $\mathbf{B}_i$ according to

$$\mathbf{E}(\mathbf{x}) = 2\hat{\mathbf{n}}(\hat{\mathbf{n}}\cdot\mathbf{E}_i(\mathbf{x})), \quad \mathbf{B}(\mathbf{x}) = 2\mathbf{B}_i(\mathbf{x}) - 2\hat{\mathbf{n}}(\hat{\mathbf{n}}\cdot\mathbf{B}_i(\mathbf{x})).$$

On substituting these equations into Eqs. (3) and (4), one thus finds

$$\mathbf{E}(\mathbf{x}_P) = \frac{1}{2\pi}\int_{\mathrm{OAP}} [ik(\hat{\mathbf{n}}\times\mathbf{B}_i)G + (\hat{\mathbf{n}}\cdot\mathbf{E}_i)\nabla G]\mathrm{d}A, \tag{6}$$

$$\mathbf{B}(\mathbf{x}_P) = \frac{1}{2\pi}\int_{\mathrm{OAP}} [(\hat{\mathbf{n}}\cdot\nabla G)\mathbf{B}_i - (\mathbf{B}_i\cdot\nabla G)\hat{\mathbf{n}}]\mathrm{d}A. \tag{7}$$

From Eq. (5) the gradient of G can be easily calculated as

$$\nabla G(\mathbf{x}) = ik\left(1 - \frac{1}{iku}\right)\frac{G(\mathbf{u})}{u}\mathbf{u}, \tag{8}$$

with $\mathbf{u} = \mathbf{x} - \mathbf{x}_P$ and $u = |\mathbf{u}|$. Moreover, if we use x and y as parameters for identifying the points on the paraboloid surface, we can easily calculate the area element and the normal to the surface:

$$dA = \sqrt{1 + s(x,y)}dxdy, \tag{9}$$

$$\hat{\mathbf{n}} = \frac{1}{\sqrt{1+s(x,y)}}\begin{pmatrix} -x/2f \\ -y/2f \\ 1 \end{pmatrix} = \frac{1}{\sqrt{1+s(x,y)}}\mathbf{p}, \tag{10}$$

where we have defined the vector $\mathbf{p} = (-x/2f, -y/2f, 1)$, which will be useful later.

We now consider an incident beam with a planar wavefront and a super-Gaussian transverse amplitude profile, to be specified below. These two assumptions are of course an approximation of a real laser beam as far as we limit ourselves to the near-field region, as in a practical real case; we also assume that no wavefront aberration affects the incident beam. Furthermore, we let the beam propagate at an arbitrary angle with respect to the paraboloid optical axis. It is then useful to introduce a new system of coordinates $O'\xi\eta\zeta$ oriented with the beam, and in particular such that (see the inset of Fig. 1):

(a) The wavevector points toward the negative ζ axis direction: $\mathbf{k} = -k\hat{\mathbf{e}}_\zeta$, with $k = 2\pi/\lambda > 0$.
(b) The "center of mass" of the transverse field amplitude profile lies in the ζ axis, that is, at $\xi = \eta = 0$.
(c) The origin O' lies on the parabola surface at the point $(d_{\mathrm{OAD}}, 0, ad_{\mathrm{OAD}}^2)$ (the OAP "center").
(d) If the propagation occurs along a direction parallel to the parabola axis (that is, if no misalignment occurs), the axes ξ, η, ζ are oriented in the same direction as x, y, z, respectively.

According to a) and b), from the Maxwell equations it follows that the fields of the incoming beam at a generic reference plane $\zeta = \zeta_0$ (located at a distance ζ_0 from the parabola center) can be written, in the $O'\xi\eta\zeta$ system, as

$$\mathbf{E}(\xi,\eta,\zeta_0) = A(\xi,\eta)[\cos\delta\hat{\mathbf{e}}_\xi + \sin\delta\hat{\mathbf{e}}_\eta], \tag{11}$$

$$\mathbf{B}(\xi,\eta,\zeta_o) = A(\xi,\eta)[-\cos\delta\hat{\mathbf{e}}_\eta + \sin\delta\hat{\mathbf{e}}_\xi], \tag{12}$$

where we have introduced the angle δ to allow for different polarizations: $\delta = 0$ corresponds to an incoming beam polarized along ξ (that is, for a perfectly aligned beam, along x). Furthermore, $A(\xi,\eta)$ accounts for the beam amplitude. We assume a super-Gaussian type beam profile, with

$$A(\xi,\eta) = A_0\exp\left[-\frac{1}{2}\left(\left(\frac{\xi}{\sigma_x}\right)^2 + \left(\frac{\eta}{\sigma_y}\right)^2\right)^n\right]. \tag{13}$$

The fields on the parabola surface can then be calculated starting from Eqs. (11) and (12) and considering the optical path from this plane to the OAP surface at each point. To this purpose, let us introduce now a new system of coordinates

$O'x'y'z'$ as shown in Fig. 1. It is simply obtained from the corresponding unprimed system $Oxyz$ by translating the origin to O'. In order to quantitatively define a generic misalignment of the incident beam with respect to the parabola axis, we now start from an $O'\xi\eta\zeta$ system aligned with $O'x'y'z'$ (no misalignment) and perform first a rotation around the η axis (coincident with the y' axis) of an angle ϑ_y and then a rotation of an angle ϑ_x along the new ξ' axis (for the sake of conciseness, we have dropped any prime symbol from the symbols used for the two rotation angles, as no ambiguity exists as far as the order of rotations is taken into account). In other words, we first let the beam rotate around an axis perpendicular to the meridional plane. It is shown in Appendix A that the electric and magnetic fields at the point $\mathbf{x}_S = (x, y, a(x^2 + y^2))$ on the paraboloid surface can thus be written as

$$\mathbf{E}_i(\mathbf{x}_S) = A(\xi(\mathbf{x}_S), \eta(\mathbf{x}_S))e^{ikp(\mathbf{x}_S)}\mathbf{q}(\delta, \vartheta_x, \vartheta_y), \tag{14}$$

$$\mathbf{B}_i(\mathbf{x}_S) = A(\xi(\mathbf{x}_S), \eta(\mathbf{x}_S))e^{ikp(\mathbf{x}_S)}\mathbf{r}(\delta, \vartheta_x, \vartheta_y), \tag{15}$$

with

$$\xi(\mathbf{x}_S) = (x - d_{\mathrm{OAD}})\cos\vartheta_y - (a(x^2 + y^2) - ad_{\mathrm{OAD}}^2))\sin\vartheta_y, \tag{16}$$

$$\eta(\mathbf{x_S}) = y\cos\vartheta_x + (a(x^2 + y^2) - ad_{\mathrm{OAD}}^2)\sin\vartheta_x\cos\vartheta_y + (x - d_{\mathrm{OAD}})\sin\vartheta_x\sin\vartheta_y \tag{17}$$

and

$$p(\mathbf{x}_S) = \zeta_0 - (a(x^2 + y^2) - ad_{\mathrm{OAD}}^2)\cos\vartheta_x\cos\vartheta_y - (x - d_{\mathrm{OAD}})\cos\vartheta_x\sin\vartheta_y + y\sin\vartheta_x. \tag{18}$$

In Eqs. (14) and (15) we have introduced the vectors $\mathbf{q}$ and $\mathbf{r}$, whose components, calculated in Appendix A, are the following:

$$\begin{aligned} q_x(\delta, \vartheta_x, \vartheta_y) &= \cos\delta\cos\vartheta_y + \sin\delta\sin\vartheta_x\sin\vartheta_y \\ q_y(\delta, \vartheta_x, \vartheta_y) &= \sin\delta\cos\vartheta_x \\ q_z(\delta, \vartheta_x, \vartheta_y) &= \sin\delta\sin\vartheta_x\cos\vartheta_y - \cos\delta\sin\vartheta_y, \end{aligned} \tag{19}$$

$$\begin{aligned} r_x(\delta, \vartheta_x, \vartheta_y) &= \sin\delta\cos\vartheta_y - \cos\delta\sin\vartheta_x\sin\vartheta_y \\ r_y(\delta, \vartheta_x, \vartheta_y) &= -\cos\delta\cos\vartheta_x \\ r_z(\delta, \vartheta_x, \vartheta_y) &= -(\cos\delta\sin\vartheta_x\cos\vartheta_y + \sin\delta\sin\vartheta_y). \end{aligned} \tag{20}$$

We have made explicit that they do not depend upon the point $\mathbf{x}_S$, but only upon the angles defining the beam misalignment and the beam polarization.

On substituting these equations into Eq. (6) we finally get

$$E_j(\mathbf{x}_P) = \frac{i}{\lambda}\int_{\mathrm{OAP}} g_{Ej}(\mathbf{x}, \mathbf{x}_P)A(\xi(\mathbf{x}), \eta(\mathbf{x}))e^{ik(u(\mathbf{x},\mathbf{x}_P)+p(\mathbf{x}))}\mathrm{d}x\mathrm{d}y, \tag{21}$$

where the index j stands for x, y, or z and

$$g_{Ex}(\mathbf{x}, \mathbf{x}_P) = \frac{1}{u(\mathbf{x}, \mathbf{x}_P)}\left(-\frac{y}{2f}r_z - r_y\right) + \left(-\frac{x}{2f}q_x - \frac{y}{2f}q_y + q_z\right) \times \left(1 - \frac{1}{iku(\mathbf{x}, \mathbf{x}_P)}\right)\frac{x - x_P}{u^2(\mathbf{x}, \mathbf{x}_P)}, \tag{22}$$

$$g_{Ey}(\mathbf{x}, \mathbf{x}_P) = \frac{1}{u(\mathbf{x}, \mathbf{x}_P)}\left(r_x + \frac{x}{2f}r_z\right) + \left(-\frac{x}{2f}q_x - \frac{y}{2f}q_y + q_z\right) \times \left(1 - \frac{1}{iku(\mathbf{x}, \mathbf{x}_P)}\right)\frac{y - y_P}{u^2(\mathbf{x}, \mathbf{x}_P)}, \tag{23}$$

$$g_{Ez}(\mathbf{x}, \mathbf{x}_P) = \frac{1}{u(\mathbf{x}, \mathbf{x}_P)}\left(-\frac{x}{2f}r_y + \frac{y}{2f}r_x\right) + \left(-\frac{x}{2f}q_x - \frac{y}{2f}q_y + q_z\right) \times \left(1 - \frac{1}{iku(\mathbf{x}, \mathbf{x}_P)}\right)\frac{z - z_P}{u^2(\mathbf{x}, \mathbf{x}_P)}. \tag{24}$$

Here z has to be replaced by $a(x^2 + y^2)$ wherever it appears. We observe that Eqs. (22)–(24) can be cast into a more compact form as

$$\mathbf{g}_E(\mathbf{x}, \mathbf{x}_P) = \frac{1}{u}(\mathbf{p}\times\mathbf{r}) + (\mathbf{p}\cdot\mathbf{q})\left(1 - \frac{1}{iku}\right)\frac{\mathbf{u}}{u^2}. \tag{25}$$

The corresponding expressions for $B_j(\mathbf{x}_p)$ are reported in Appendix B.

In the following Section, we use the above model to calculate how the maximum intensity and Strehl ratio are affected by small misalignments for a variety of OAP off-axis angles and focal lengths. We defer until Section 4 a discussion of a set of experimental measurements aimed at assessing the validity of our model.

3. CALCULATION AND DISCUSSION OF SELECTED CASES

The integrals appearing in Eq. (21) have, as it is easily verified, no closed form and need to be calculated numerically. In our case, where incoming beam misalignments are accounted for, this is a particularly heavy task, due to the number of terms appearing in Eqs. (16), (17) and (22)–(24). Several numerical algorithms have been developed to estimate integrals involving highly oscillating terms [30–33]; in our case a Levin method was chosen [34]. In particular, since we are interested here in the calculation of the intensity profile of the beam at the final plane (from now on, by "final plane" we mean either the focal or some other plane in the far-field region to be specified in the following), we calculated the three components of the electric field provided by Eq. (21) using a Levin method and then we summed up the squared values. All the calculations referred to below were carried out assuming a beam with wavelength $\lambda = 800$ nm, polarization along the ξ axis [$\delta = 0$ in

Eqs. (11) and (12)], and transverse profile as provided by Eq. (13) with $n = 4$. We choose these figures as they are typically encountered in ultrashort/ultraintense laser–matter interaction experiments. Furthermore, the extent of the numerical integration domain was typically taken as 3 × FWHM in both the x and y directions, being the full width at half-maximum (FWHM) of the beam to be focused. In all the calculations discussed here, we consider a beam with FWHM = 10 mm along both the ξ and η directions [$\sigma_\xi = \sigma_\eta$ in Eq. (13)]. With the above parameters, the calculation of each field component at a given point of the final plane took from a few up to ≈10 s on a single core of a typical desktop CPU (up to 4 cores were used, in our case, to speed up the calculations).

As an example, Figs. 2 and 3 show the retrieved beam intensity map at the focal plane of an $f/10$ OAP with an off-axis angle $\vartheta_{OA} = 20°$, for different misalignment angles ϑ_x and ϑ_y (from now on, since we are not accounting for a time dependence, we will improperly use the term "intensity" to refer to the electromagnetic energy density). All the maps shown in Figs. 2 and 3 are centered on the position of an ideal ray reflected from the OAP center (point O' in Fig. 1); in other words, on each map the coordinate (0, 0) corresponds to the point where this ideal reflected ray would intercept the focal plane. In detail, Fig. 2 shows, besides the focal spot image of a perfectly aligned beam, the intensity profile for increasing misalignments around the x axis, with positive ϑ_x values up to 3.0° (due to the symmetry of the system, the cases with negative ϑ_x values are similar). Figure 3 shows, instead, the intensity profiles for

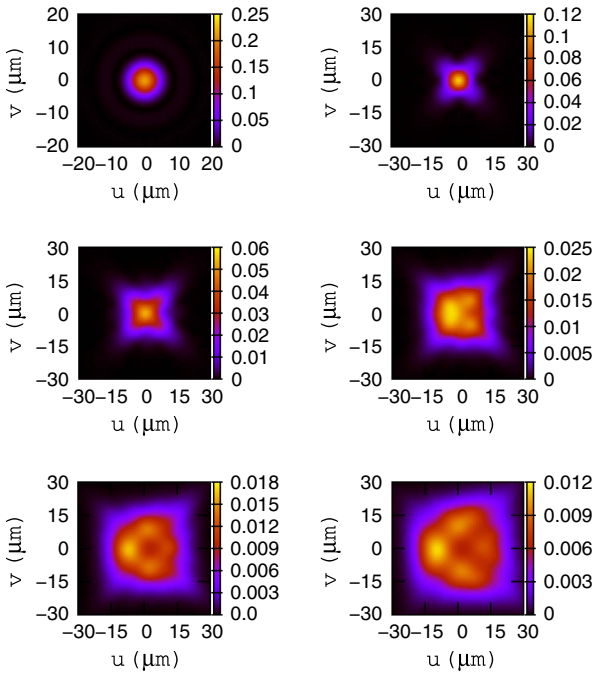

Fig. 2. Intensity distributions in the focal plane for an $f/10$, $\vartheta_{OA} = 20°$ OAP, calculated for a perfectly aligned beam (top left) and for increasing misalignments around the x axis; from top left to bottom right: $\vartheta_x = 0°$, $\vartheta_x = +1.0°$ (first line), $\vartheta_x = +1.5°$, $\vartheta_x = +2.0°$ (second line), $\vartheta_x = +2.5°$, $\vartheta_x = +3.0°$ (third line). $\vartheta_y = 0°$ in all the cases shown. The coordinates u and v are defined in Fig. 1. Notice the different spatial scales for the perfect alignment case.

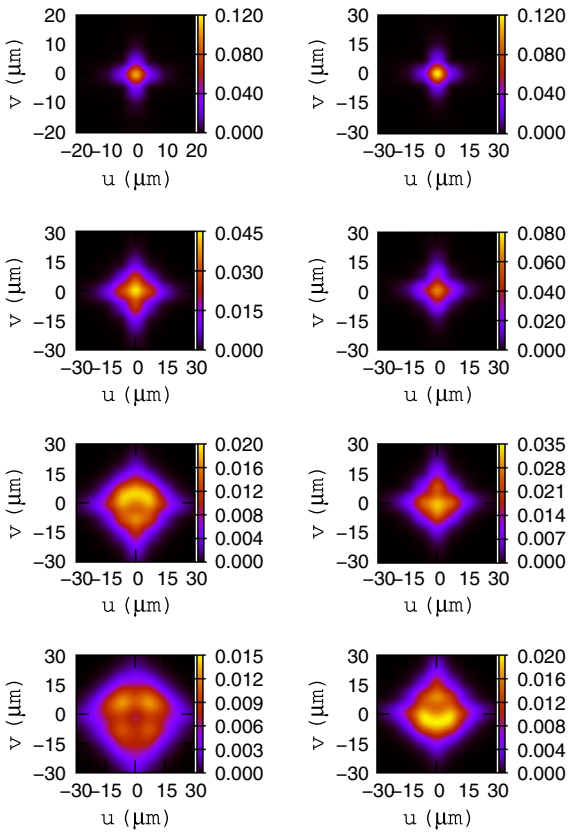

Fig. 3. Intensity distributions in the focal plane for an $f/10$, $\vartheta_{OA} = 20°$ OAP, calculated for increasing positive (left column) and negative (right column) misalignments around the y axis; from top to bottom: $\vartheta_y = \pm 1.0°$ (first line), $\vartheta_y = \pm 1.5°$ (second line), $\vartheta_y = \pm 2.0°$ (third line), $\vartheta_y = \pm 2.5°$ (fourth line). $\vartheta_x = 0°$ in all the cases shown. The coordinates u and v are defined in Fig. 1. Notice the different spatial scales for the perfect alignment case.

increasing ϑ_y values, up to 2.5° (for both positive and negative values). Each 2D intensity map was typically sampled with a $\lesssim \lambda/2$ resolution (depending on the OAP f number, that is, on the expected waist size). For instance, each of the maps shown in Figs. 2 and 3 were sampled with a 0.4 μm resolution; thus, the number of sampling points for each map was $n_{sampling} \approx 22500$, resulting in a few hours calculation time on a single-core CPU.

Increasing astigmatism- and coma-like aberrations are clearly visible in Figs. 2 and 3 as the angles of misalignment increase; actually, these kinds of aberrations were shown to be inherent to the off-axis configuration even for perfectly aligned beams [21,22]. Rather than characterizing the aberrations by retrieving, for instance, the Zernike coefficients [35], we are interested here in studying the maximum intensity and the Strehl ratio as a function of the misalignment angles; here, by "maximum intensity" we mean the maximum value of the intensity reached in the focal plane. It is worth observing, at this point, that a treatment of the misalignments based upon a scalar diffraction theory could be sufficient for a study of the maximum intensity and Strehl ratio, in particular at large f numbers. As a matter of fact, we mention here that we actually run some sets of simulations with a beam polarized along η,

which resulted in no differences with respect to the cases discussed in the following. Relying on a scalar theory would both simplify the equations and allow faster numerical simulations to be performed. Nevertheless, we believe that the possibility of studying the polarization patterns, which is outside the scope of the present paper, provides a solid motivation for a vector diffraction theory to be available.

As it will be clear in the following, noticeable deviations from the ideal values of both maximum intensity and Strehl ratio (that is, the ones achievable with a perfectly aligned beam) actually result from much smaller angles of misalignment than those considered in Figs. 2 and 3. In particular, in the following we will discuss some selected cases with the aim of drawing some general conclusions about the stability of these values, under small misalignments, for different OAP parameters such as the f number and the off-axis angle ϑ_{OA}. To this purpose, we run several intensity map calculations of the kind of those shown above and then retrieved, from each map, the maximum intensity (I_{max}) and the Strehl ratio (SR); each point in the plots of Figs. 4, 6, and 7 thus corresponds to a full intensity map calculation. We notice here that, in order to estimate the Strehl ratio for each misalignment angle pair (ϑ_x, ϑ_y), we first calculated the total energy contained into the beam region where the intensity $I(u, v)$ is greater than $0.1 \times I_{max}$ and then divided this value by the corresponding value for the case of no misalignment ($\vartheta_x = 0, \vartheta_y = 0$). A similar convention was used in [24] (see [35] for a more formal definition).

Figure 4 shows the behavior of I_{max} and SR in the case of an $f/10$ OAP with an off-axis angle $\vartheta_{OA} = 20°$. Misalignments around x ($\vartheta_y = 0$) and y ($\vartheta_x = 0$) are considered separately, and shown in the top and bottom line, respectively. The plots corresponding to misalignments around the x axis are symmetric around $\vartheta_x = 0$, as it is easily guessed from Fig. 1 (from now on, for the sake of conciseness, we will refer to a misalignment around x as an "x misalignment," and similarly for y).

The plots show that a ≈20% drop of the maximum intensity occurs for angle values of ≈0.6°, whereas a much smaller drop (≈7%) is observed in the Strehl ratio over the same range

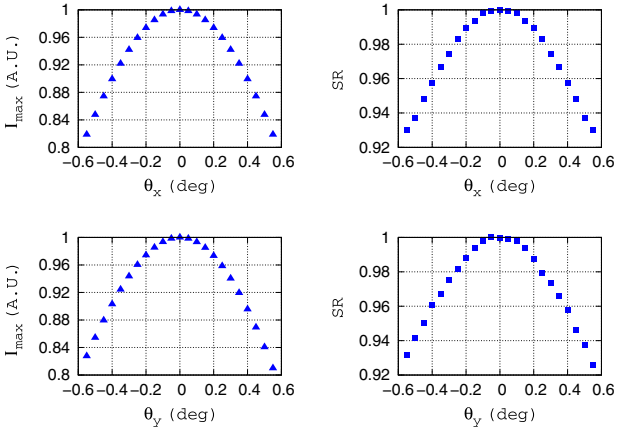

Fig. 4. Plots of the I_{max} (left column) and of the SR (right column) as a function of the misalignment angle for a misalignment around the x axis (top line) and around the y axis (bottom line), for an $f/10$, $\vartheta_{OA} = 20°$ OAP.

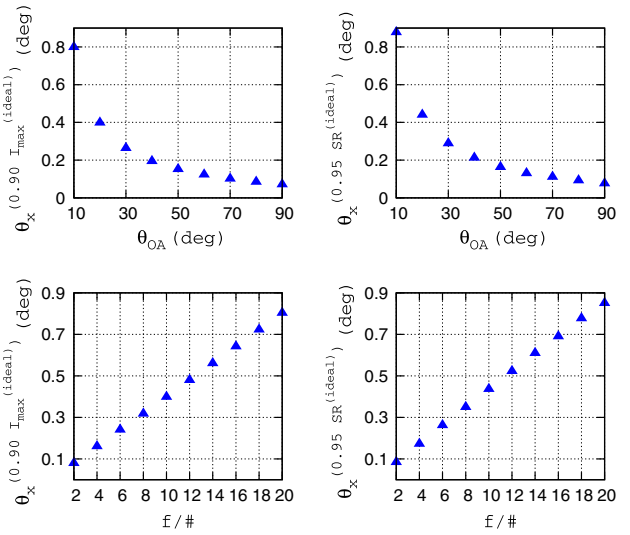

Fig. 5. *Top line*: critical ϑ_x angles (for a counterclockwise rotation misalignment), resulting in a 10% decrease of the maximum intensity (left) and a 5% decrease of the Strehl ratio (right), as a function of the parabola off-axis angle ϑ_{OA} (at $f/\# = 10$). *Bottom line*: critical ϑ_x angles (for a counterclockwise rotation misalignment), resulting in a 10% decrease of the maximum intensity (left) and a 5% decrease of the Strehl ratio (right), as a function of the parabola f number (at $\vartheta_{OA} = 20°$).

of misalignment angles. We notice that the misalignment angles considered here are much smaller than those considered in Figs. 2 and 3.

In order to assess the dependence of these effects upon the OAP off-axis angle, we run different sets of simulations (at a given f number) and we retrieved, for each set, the misalignment angles corresponding to a 10% drop of the maximum intensity and to a 5% drop of the Strehl ratio (for the sake of brevity, we will be calling these "critical angles" for the intensity and Strehl ratio, respectively). In the top line of Fig. 5 we plot these angles as a function of the OAP off-axis angle ϑ_{OA}, in the case of a counterclockwise ($\vartheta_x > 0$) misalignment around x. As it is clear from Fig. 5, the tolerances of I_{max} and SR towards small misalignments quickly decrease as the off-axis angle ϑ_{OA} increases. These plots were fitted with a curve of the type $\vartheta_{crit} \propto 1/\vartheta_{OA}^{\alpha}$; the retrieved α coefficients in each case are shown in Table 1, where the values of the α coefficient for y misalignment (whose plots are not shown for the sake of brevity) are reported as well. These coefficients basically provide a scaling law for the tolerances of the intensity and Strehl ratio to small misalignments as a function of the parabola off-axis angle. We observe that the increase of the sensitivity to small misalignments of both the intensity and the Strehl ratio as a function of the off-axis angle is faster for misalignment around x than for misalignment around y.

A set of analogous plots to those of Fig. 4 is shown in Fig. 6 for a smaller f number OAP ($f/2$ against $f/10$) and the same off-axis angle ($\vartheta_{OA} = 20°$). Here it is clearly visible that smaller misalignment angles, both in the case of x and y misalignments, are enough to result in similar drops of both I_{max} and SR than in the case of the higher f number OAP; this is a consequence

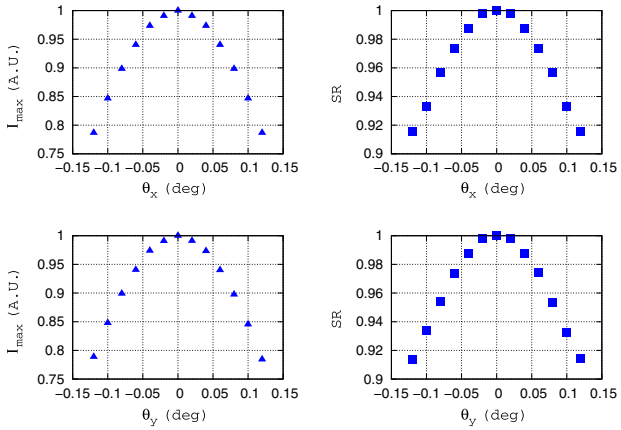

Fig. 6. Plots of the $I_{\max}$ (left column) and of the SR (right column) as a function of the misalignment angle for a misalignment around the x axis (top line) and around the y axis (bottom line), for an $f/2$, $\vartheta_{\mathrm{OA}} = 20°$.

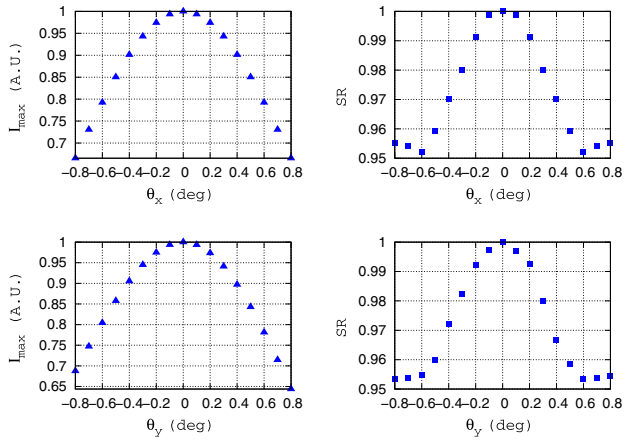

Fig. 7. Plots of the $I_{\max}$ (left column) and of the SR (right column), calculated on a plane placed at a distance $1 \times d_R$ before the focal plane, as a function of the misalignment angle, for a misalignment around the x axis (top line) and around the y axis (bottom line), for an $f/10$, $\vartheta = 20°$ OAP.

of the fact that a smaller f number results, at a given off-axis angle, in a higher astigmatism. In the bottom line of Fig. 5 we show the dependence of the critical angles for the intensity and Strehl ratio (that is, we remind, the angles resulting in a 10% and 5% drop in the $I_{\max}$ and SR, respectively) as a function of the OAP f number (at a fixed off-axis angle $\vartheta_{\mathrm{OA}} = 20°$). Again, this plot corresponds to counterclockwise ($\vartheta_x > 0$) misalignment around the x axis, while the corresponding plots for y misalignments are not shown for the sake of brevity. These plots were fitted with a linear function $\vartheta_{\mathrm{crit}} = a + b(f/\#)$. Similar trends were found for misalignments around the y axis. The slope coefficients b for both the x and y misalignments are shown in Table 1.

Finally, we show in Fig. 7 a set of plots similar to those of Fig. 4 where the beam transverse profile at a plane placed at a distance $1 \times d_R$ before the focus position is considered (here d_R is the Rayleigh length). As already said in the introduction, the beam profile at positions different from the best focus is useful to be known in laser–matter interaction experiments. It is easily seen from the figure that similar drops of both the intensity and Strehl ratio are to be expected, due to x or y misalignments, out of the focal plane too.

Table 1. Power (α) Coefficients of the Power Law $\vartheta_{\mathrm{crit}} \propto 1/\vartheta^{\alpha}$ Fitting the Data of the Critical Angles Versus the Parabola Off-axis Angle (See Top Line of Fig. 5) and Slope (b) Coefficients of the Linear Function $\vartheta_{\mathrm{crit}} = a + b \times (f/\#)$ Fitting the Data of the Critical Angles Versus the Parabola f Number (See Bottom Line of Fig. 5)

Quantity	α	Quantity	α
$\vartheta_x^{(0.90 I_{\max})}$	0.94 ± 0.08	$\vartheta_y^{(0.90 I_{\max})}$	0.86 ± 0.03
$\vartheta_x^{(0.95\mathrm{SR})}$	0.93 ± 0.07	$\vartheta_y^{(0.95\mathrm{SR})}$	0.84 ± 0.04
Quantity	b	**Quantity**	b
$\vartheta_x^{(0.90 I_{\max})}$	0.039 ± 0.0002	$\vartheta_y^{(0.90 I_{\max})}$	0.046 ± 0.0005
$\vartheta_x^{(0.95\mathrm{SR})}$	0.039 ± 0.0001	$\vartheta_y^{(0.95\mathrm{SR})}$	0.049 ± 0.0001

4. EXPERIMENTAL TEST OF THE MODEL

In this Section, we will report on a set of experimental measurements aimed at assessing the validity of the model developed in Section 2. The measurements were carried out at the Intense Laser Irradiation Laboratory of the Istituto Nazionale di Ottica of the Italian National Research Council in Pisa, Italy, where an ultrashort and ultraintense 10 TW laser system is available for studies in the field of laser-driven particle acceleration and the development of secondary sources (see, for instance, [36]). In particular, the laser can deliver <40 fs pulses with up to 450 mJ energy, at a 10 Hz repetition rate. For the present study, the laser system was operated at very low energy ($\lesssim$1 mJ) and focused by means of a long focal length OAP routinely used for laser wakefield acceleration studies. In particular, this OAP features an f number close to 11 and an off-axis angle $\vartheta_{\mathrm{OA}} \simeq 23.5°$.

A sketch of the experimental setup inside the vacuum chamber usually hosting the OAP and the gas target (not shown in figure) is shown in Fig. 8. For the present set of measurements, an Ag-coated mirror was inserted after the OAP in front (that is, upstream) of the target, to send the beam focused by the OAP to an imaging system made up by a microscope objective and a CCD, 8-bit ADC camera. The magnification was measured to be ~20. The camera pixel size was 5 μm × 5 μm. Both x and y misalignments were separately introduced (in the case of the setup shown in the figure, the y axis is normal to the plane of the figure and the x axis lies on this plane). A typical image of the focal spot of the beam in the case of a perfect alignment is shown in the inset of Fig. 8. Since the direction of the focused beam was expected to change according to the angle of misalignment considered, the last mirror was used to bring this direction back to the optical axis of the imaging system on each shot. Moreover, since noticeable shot-to-shot fluctuations, of the order of 10% of the laser energy were to be expected at the low amplification level used, each measurement was normalized to the effective laser shot energy.

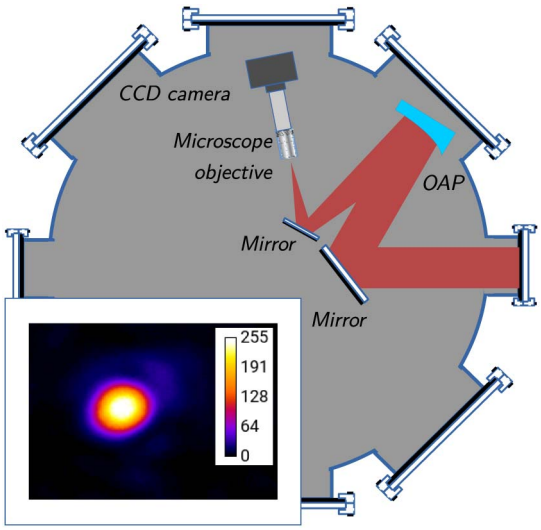

Fig. 8. Sketch of the setup used to experimentally validate our model. In the inset, an image of the perfectly aligned focal spot is shown.

Figure 9 shows the experimental results for the maximum intensity (left column) and the Strehl ratio (right column) in the case of x (top line) and y (bottom line) misalignments. The Strehl ratio was calculated as described in the previous section. It is worth noting that in this "real" case, the retrieved value should be more properly defined as a "Strehl ratio worsening" with respect to the effective Strehl ratio (smaller than 1) at no misalignment; for the sake of brevity, we will just use the term "Strehl ratio" in the following.

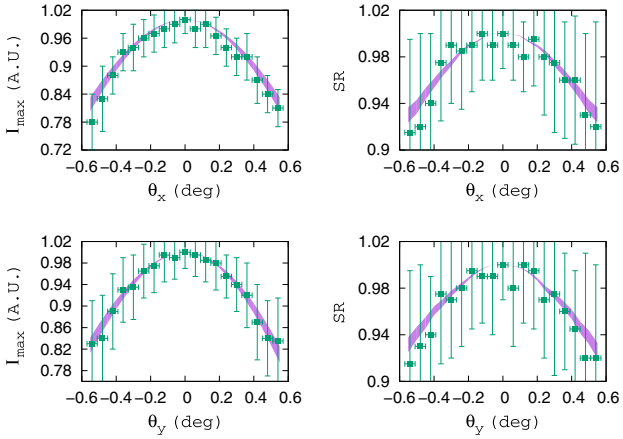

Fig. 9. Plots of the relative intensity (left column) and the Strehl ratio (right column), both measured against the reference value at no misalignment. Misalignments around x and y are considered in the top and bottom line, respectively. (Please note that, in order to keep the readability of the plots as high as possible, the vertical scale of the plots was not enlarged to accommodate the entire height of the vertical error bars; however, these error bars are to be considered symmetric around each point, so that they can be retrieved from the plots.) The shadowed regions show the regions bounded by the theoretical curves corresponding to a beam with wavelength 780 nm (lower bound) and 820 nm (upper bound).

In order to compare the experimental results with the predictions of our model, we run numerical simulations with the parameters corresponding to the used OAP. However, it is to be noticed here that the ultrashort laser beam used featured a pretty large bandwidth, roughly spanning the range from 780 to 820 nm. Of course, a thorough treatment of the issue would require an improvement of our model to take into account the ultrashort duration and large bandwidth; this is beyond the scope of the present paper and will be the subject of a future work. Here, we choose a simpler approach, running two sets of simulations, each corresponding to the boundary wavelength of the laser pulse bandwidth, namely 780 and 820 nm. The shadowed region in the plots of Fig. 9 is thus the region bounded by the curves corresponding to these two wavelengths. We observe, by the way, that the lower bound (indicating a higher sensitivity to misalignments) corresponds to the lower (780 nm) wavelength. As it appears from the plots, the agreement between the experimental points and the predictions from our model is rather good, although a pretty large scatter of the experimental points is to be noticed, in particular in the values retrieved for the Strehl ratios. This may be partly due to the limited dynamic range of our CCD camera. Moreover, it is to be noticed that our calculations strictly hold in the case of no wavefront aberrations, which is not the case for such a real beam (for instance, in our case the M^2 value, one of the parameters affected by the transverse wavefront, is close to 1.5). This is, of course, one of the reasons why the Strehl ratio is usually measured in a rather different way, by retrieving it from transverse wavefront measurements carried out, for instance, using Shack–Hartmann sensors. However, it is worth pointing out at this stage that our model can be easily generalized to cope with beams affected by transverse aberrations; indeed, this can be done by considering a transverse phase profile on the OAP surface as resulting by an impinging wavefront not perfectly plane.

5. SUMMARY AND CONCLUSIONS

In this paper, a general procedure was outlined to calculate the degradation of the maximum intensity and of the Strehl ratio of a beam focused by an off-axis parabolic mirror due to small misalignments of the initial beam with respect to the parent parabola axis. In particular, the procedure described here, based upon the vector diffraction Stratton–Chu formulas, allows the beam transverse profile at different positions of the focal region of a not perfectly aligned off-axis parabola to be evaluated numerically, whence the maximum available intensity and the Strehl ratio (calculated against a perfectly aligned beam) can be retrieved.

A formal establishment of the problem in the presence of a general misalignment was first given, aimed at providing some useful formulas to be used in the general case. Afterward, the procedure was used to carry out a sensitivity analysis of both the intensity and the Strehl ratio for a range of different focusing conditions. In particular, since this analysis was aimed at highlighting, whenever possible, the dependence of the effects of misalignments upon the OAP parameters, a parametric study was carried out at different f numbers and off-axis angles and some final phenomenological relationships have been provided.

This work can be helpful, in particular, in the design of ultrashort and ultraintense laser–matter interaction experiments. Indeed, in this context, very small misalignments as those encountered in this paper may easily affect the effective values of both the intensity and Strehl ratio; hence, a careful account of those technological issues related to the beam transport and focusing has to be made, in particular for large scale laser systems, involving long beam paths and complex setups.

APPENDIX A: FIELDS CALCULATION ON THE PARABOLOID SURFACE

We will briefly show in the following how the Eqs. (14)–(18), providing the electric and magnetic fields on the OAP surface, can be retrieved. We will focus on the electric field, as the calculation of the magnetic field proceeds in a similar fashion.

In order to calculate the quantities appearing in Eq. (11) in a point on the OAP surface, it is convenient to work in the system $O'\xi\eta\zeta$, introduced in Section 2. Recalling how the new system was obtained starting from $Oxyz$, it is easy to write down the affine transformation relating the (contravariant) components of a vector representing the same point in the two systems:

$$\mathbf{x}^{(\xi\eta\zeta)} = R_x(\vartheta_x)R_y(\vartheta_y)(\mathbf{x}^{(xyz)} - \mathbf{x}_0) \equiv A(\mathbf{x}^{(xyz)} - \mathbf{x}_0), \tag{A1}$$

with $\mathbf{x}_0 = (d_{\mathrm{OAD}}, 0, ad_{\mathrm{OAD}}^2)$, $A = R_x(\vartheta_x)R_y(\vartheta_y)$ and

$$R_y(\vartheta_y) = \begin{pmatrix} \cos\vartheta_y & 0 & -\sin\vartheta_y \\ 0 & 1 & 0 \\ \sin\vartheta_y & 0 & \cos\vartheta_y \end{pmatrix}, \tag{A2}$$

$$R_x(\vartheta_x) = \begin{pmatrix} 1 & 0 & 0 \\ 0 & \cos\vartheta_x & \sin\vartheta_x \\ 0 & -\sin\vartheta_x & \cos\vartheta_x \end{pmatrix}. \tag{A3}$$

As said in the text, we have dropped here any prime symbol from ϑ_x and ϑ_y, as no ambiguity exists as far as the order of the rotations is kept into account. We thus consider the electric field at the generic surface point having coordinates $\mathbf{x}_S^{(\xi\eta\zeta)} = (\xi_S, \eta_S, \zeta_S)$ obtained from $\mathbf{x}_S = (x_S, y_S, a(x_S^2 + y_S^2))$ by the transformation [Eq. (A1)]. Looking at Eq. (11), it is easy to write down the field on the surface as

$$\mathbf{E}(\mathbf{x}_S^{(\xi\eta\zeta)}) = A(\xi_S, \eta_S)e^{ikp(\mathbf{x}_S^{(\xi\eta\zeta)})}[\cos\delta\hat{\mathbf{e}}_\xi + \sin\delta\hat{\mathbf{e}}_\eta], \tag{A4}$$

where $p(\mathbf{x}_S^{(\xi\eta\zeta)})$ is the optical path from the reference plane $\zeta = \zeta_0$ to the surface point $\mathbf{x}_S^{(\xi\eta\zeta)}$. Since we assume a propagation in vacuum, this is just the distance between the plane and the point; taking into account that the beam is propagating in the negative ζ direction, it can be directly obtained as the difference between ζ_0 and the third component of $\mathbf{x}_S^{(\xi\eta\zeta)}$, and carrying out this calculation leads to Eq. (18).

As for the field amplitude $A(\xi_S, \eta_S)$, it is simply given by $A(\xi, \eta)$ as defined in Eq. (13), calculated at the point $\mathbf{x}_S^{(\xi\eta\zeta)}$ [which depends on $\mathbf{x}_S^{(xyz)}$ through Eq. (A1)], which, after some cumbersome algebra, leads to Eqs. (16) and (17).

Finally, in order to evaluate the Stratton–Chu integral, we must express the electric field direction as a function of the base vectors $\hat{\mathbf{e}}_x$, $\hat{\mathbf{e}}_y$, $\hat{\mathbf{e}}_z$. To this purpose, the base vectors $\hat{\mathbf{e}}_\xi$, $\hat{\mathbf{e}}_\eta$, $\hat{\mathbf{e}}_\zeta$ must be expressed in terms of $\hat{\mathbf{e}}_x$, $\hat{\mathbf{e}}_y$, $\hat{\mathbf{e}}_z$. One of the ways is, for instance, to consider that, apart from a translation by $\mathbf{x}_0$, not affecting the directions of the axes unit vectors, the two bases of $Oxyz$ and $O'\xi\eta\zeta$ transform as the covariant components of a vector, that is, when arranged in a column vector (see, for instance, [37]),

$$\begin{pmatrix} \hat{\mathbf{e}}_\xi \\ \hat{\mathbf{e}}_\eta \\ \hat{\mathbf{e}}_\zeta \end{pmatrix} = A^{-1T} \begin{pmatrix} \hat{\mathbf{e}}_x \\ \hat{\mathbf{e}}_y \\ \hat{\mathbf{e}}_z \end{pmatrix}. \tag{A5}$$

On substituting these relations into Eq. (11), one finally gets the Eqs. (19) and (20).

APPENDIX B: EXPRESSION OF THE MAGNETIC FIELD

For the sake of completeness, we provide here the analog of Eq. (21) for the magnetic field:

$$B_j(\mathbf{x}_P) = \frac{i}{\lambda}\int_{\mathrm{OAP}} g_{Bj}(\mathbf{x}, \mathbf{x}_P)A(\xi(\mathbf{x}, \eta(\mathbf{x}))e^{ik(u(\mathbf{x},\mathbf{x}_P)+p(\mathbf{x}))}\mathrm{d}x\mathrm{d}y, \tag{B1}$$

where

$$g_{Bx}(\mathbf{x}, \mathbf{x}_P) = \left(1 - \frac{1}{iku}\right)\frac{1}{u^2} \times \left[\left(-\frac{y}{2f}r_x + \frac{x}{2f}r_y\right)(y - y_P) + \left(r_x + \frac{x}{2f}r_z\right)(z - z_P)\right], \tag{B2}$$

$$g_{By}(\mathbf{x}, \mathbf{x}_P) = \left(1 - \frac{1}{iku}\right)\frac{1}{u^2} \times \left[\left(-\frac{x}{2f}r_y + \frac{y}{2f}r_x\right)(x - x_P) + \left(r_y + \frac{y}{2f}r_z\right)(z - z_P)\right], \tag{B3}$$

$$g_{Bz}(\mathbf{x}, \mathbf{x}_P) = \left(1 - \frac{1}{iku}\right)\frac{1}{u^2} \times \left[\left(-\frac{x}{2f}r_z - r_x\right)(x - x_P) + \left(-\frac{y}{2f}r_z - r_y\right)(y - y_P)\right], \tag{B4}$$

where $z = a(x^2 + y^2)$. Similar to the expression for $\mathbf{E}$, the Eqs. (B1)–(B3) can be written in a compact form as

$$\mathbf{g}_B(\mathbf{x}, \mathbf{x}_P) = \left(1 - \frac{1}{iku}\right)\frac{1}{u^2}(\mathbf{p} \times \mathbf{r}) \times \mathbf{u}. \tag{B5}$$

Funding. Italian Ministry of Health (GR-2009-1608935 D.I. AgeNaS); CNR; PRIN (PRIN2012AY5LEL); MIUR-FIRB (SPARX); INFN gResist and Plasma-med collaborations;

Regione Toscana 09/03/2012 (protocollo ISTI-CNR No 0000745); European Union (653782–EuPRAXIA)

REFERENCES

1. M. Kempe and W. Rudolph, "Femtosecond pulses in the focal region of lenses," Phys. Rev. A **48**, 4721–4729 (1993).
2. P. Gorenstein, "High throughput X-ray optics: an overview," Appl. Opt. **27**, 1433–1439 (1988).
3. M. Umbach, V. Nazmov, M. Simon, A. Last, and V. Saile, "Achromatic X-ray focusing using diffractive and refractive elements," Proc. SPIE **7100**, 71001U (2008).
4. N. Bokor and N. Davidson, "4π focusing with single paraboloid mirror," Opt. Commun. **281**, 5499–5503 (2008).
5. J. Stadler, C. Stanciu, C. Stupperich, and A. J. Meixner, "Tighter focusing with a parabolic mirror," Opt. Lett. **33**, 681–683 (2008).
6. H. Dehez, M. Piché, and Y. De Koninck, "Enhanced resolution in two-photon imaging using a TM_{01} laser beam at a dielectric interface," Opt. Lett. **34**, 3601–3603 (2009).
7. A. April and M. Piché, "4π focusing of TM_{01} beams under nonparaxial conditions," Opt. Express **18**, 22128–22140 (2010).
8. P. Varga and P. Török, "Focus of electromagnetic waves by paraboloid mirrors. I. Theory," J. Opt. Soc. Am. A **17**, 2081–2089 (2000).
9. P. Varga and P. Török, "Focus of electromagnetic waves by paraboloid mirrors. II. Numerical results," J. Opt. Soc. Am. A **17**, 2090–2095 (2000).
10. A. Drechsler, M. A. Lieb, C. Debus, A. J. Meixner, and G. Tarrach, "Confocal microscopy with a high numerical aperture parabolic mirror," Opt. Express **9**, 637–644 (2001).
11. M. A. Lieb and A. J. Meixner, "A high numerical aperture parabolic mirror as imaging device for confocal microscopy," Opt. Express **8**, 458–474 (2001).
12. S. Quabis, R. Dorn, M. Eberler, O. Glockl, and G. Leuchs, "Focusing light to a tighter spot," Opt. Commun. **179**, 1–7 (2000).
13. R. Dorn, S. Quabis, and G. Leuchs, "Sharper focus for a radially polarized light beam," Phys. Rev. Lett. **91**, 233901 (2003).
14. A. Macchi, M. Borghesi, and M. Passoni, "Ion acceleration by super-intense laser-plasma interaction," Rev. Mod. Phys. **85**, 751–793 (2013).
15. E. Esarey, C. B. Schroeder, and W. P. Leemans, "Physics of laser-driven plasma-based electron accelerators," Rev. Mod. Phys. **81**, 1229–1285 (2009).
16. S. Corde, K. Ta Phouk, G. Lambert, R. Fitour, V. Malka, A. Rousse, A. Beck, and E. Lefebvre, "Femtosecond X-rays from laser-plasma accelerators," Rev. Mod. Phys. **85**, 1–48 (2013).
17. L. Labate, M. Galimberti, A. Giulietti, D. Giulietti, P. Köster, P. Tomassini, and L. A. Gizzi, "Study of forward accelerated fast electrons in ultrashort Ti K_α sources," Appl. Phys. B **86**, 229–233 (2007).
18. F. Baffigi, G. Cristoforetti, L. Fulgentini, A. Giulietti, P. Koester, L. Labate, and L. A. Gizzi, "X-ray conversion of ultra-short laser pulses on a solid sample: role of electron waves excited in the pre-plasma," Phys. Plasmas **21**, 072108 (2014).
19. G. Cristoforetti, A. Anzalone, F. Baffigi, G. Bussolino, G. D'Arrigo, L. Fulgentini, A. Giulietti, P. Koester, L. Labate, S. Tudisco, and L. A. Gizzi, "Investigation on laser-plasma coupling in intense, ultrashort irradiation of a nanostructured silicon target," Plasma Phys. Controlled Fusion **56**, 095001 (2014).
20. J. E. Howard, "Imaging properties of off-axis parabolic mirrors," Appl. Opt. **18**, 2714–2722 (1979).
21. P. Arguijo, M. S. Scholl, and G. Paez, "Diffraction patterns formed by an off-axis paraboloid surface," Appl. Opt. **40**, 2909–2916 (2001).
22. P. Arguijo and M. S. Scholl, "Exact ray-trace beam for an off-axis paraboloid surface," Appl. Opt. **42**, 3284–3289 (2003).
23. C. Brückner, G. Notni, and A. Tünnermann, "Optimal arrangement of 90° off-axis parabolic mirrors in THz setups," Optik **121**, 113–119 (2010).
24. A. April, P. Bilodeau, and M. Piché, "Focusing a TM(01) beam with a slightly tilted parabolic mirror," Opt. Express **19**, 9201–9212 (2011).
25. J. Burke, K. Wang, and A. Bramble, "Null test of an off-axis parabolic mirror. I. Configuration with spherical reference wave and flat return surface," Opt. Express **17**, 3196–3210 (2009).
26. S.-W. Bahk, P. Rousseau, T. A. Planchon, V. Chvykov, G. Kalintchenko, A. Maksimchuk, G. A. Mourou, and V. Yanovsky, "Characterization of focal field formed by a large numerical aperture paraboloidal mirror and generation of ultra-high intensity (10^{22}W/cm^2)," Appl. Phys. B **80**, 823–832 (2005).
27. J. A. Stratton and L. J. Chu, "Diffraction theory of electromagnetic waves," Phys. Rev. **56**, 99–107 (1939).
28. Space Optics Research Labs, 2016, website http://www.sorl.com.
29. J. D. Jackson, *Classical Electrodynamics*, 3rd ed. (Wiley, 1999).
30. F. Shen and A. Wang, "Fast-Fourier-transform based numerical integration method for the Rayleigh-Sommerfeld diffraction formula," Appl. Opt. **45**, 1102–1110 (2006).
31. J. A. C. Veerman, J. J. Rusch, and H. P. Urbach, "Calculation of the Rayleigh-Sommerfeld diffraction integral by exact integration of the fast oscillating factor," J. Opt. Soc. Am. A **22**, 636–646 (2005).
32. V. Nascov and P. C. Logofatu, "Fast computation algorithm for the Rayleigh-Sommerfeld diffraction formula using a type of scaled convolution," Appl. Opt. **48**, 4310–4319 (2009).
33. P. Török, P. R. T. Munro, and E. E. Kriezis, "Rigorous near- to far-field transformation for vectorial diffraction calculations and its numerical implementation," J. Opt. Soc. Am. A **23**, 713–722 (2006).
34. D. Levin, "Fast integration of rapidly oscillatory functions," J. Comput. Appl. Math. **67**, 95–101 (1996).
35. M. Born and E. Wolf, *Principles of Optics*, 7th ed. (Cambridge University, 1999).
36. L. A. Gizzi, L. Labate, F. Baffigi, F. Brandi, G. C. Bussolino, L. Fulgentini, P. Köster, D. Palla, and F. Rossi, "Laser-plasma acceleration of electrons for radiobiology and radiation sources," Nucl. Instrum. Methods Phys. Res. Sect. B **355**, 241–245 (2015).
37. S. Hassani, *Mathematical Physics*, 2nd ed. (Springer, 2013).